

Rydberg Atomic Receivers for Multi-Band Communications and Sensing

Mingyao Cui, Qunsong Zeng, Zhanwei Wang, and Kaibin Huang, *Fellow, IEEE*

Abstract—Harnessing multi-level electron transitions, Rydberg Atomic Receivers (RAREs) can detect wireless signals across a wide range of frequency bands, from Megahertz to Terahertz, enabling multi-band communications and sensing (C&S). Current research on multi-band RAREs primarily focuses on experimental demonstrations, lacking an interpretable model to mathematically characterize their mechanisms. This issue leaves the multi-band RARE as a black box, posing challenges in its practical C&S applications. To fill in this gap, this paper investigates the underlying mechanism of multi-band RAREs and explores their optimal performance. For the first time, the closed-form expression of the transfer function of a multi-band RARE is derived by solving the quantum response of Rydberg atoms excited by multi-band signals. The function reveals that a multi-band RARE simultaneously serves as both a *multi-band atomic mixer* for down-converting multi-band signals and a *multi-band atomic amplifier* that reflects its sensitivity to each band. Further analysis of the atomic amplifier unveils that the gain factor at each frequency band can be decoupled into a *global gain* term and a *Rabi attention* term. The former determines the overall sensitivity of a RARE to all frequency bands of wireless signals. The latter influences the allocation of the overall sensitivity to each frequency band, representing a unique attention mechanism of multi-band RAREs. The optimal design of the global gain is provided to maximize the overall sensitivity of multi-band RAREs. Subsequently, the optimal Rabi attentions are also derived to maximize the practical multi-band C&S performance. Numerical results confirm the effectiveness of the derived transfer function and the superiority of multi-band RAREs.

Index Terms—Rydberg atomic receivers, wireless communications, sensing, multi-band.

I. INTRODUCTION

The precise measurement of radio-frequency (RF) signals is fundamental to the digital age, serving as a core operation in wireless communications, remote sensing, e-health, and radar systems. Emerging from the domain of quantum sensing, the Rydberg Atomic REceiver (RARE) has recently been introduced as a new concept in high-precision wireless detection by exploiting the quantum properties of Rydberg atoms [1]–[6]. Specifically, Rydberg atoms are highly excited atoms wherein one or more electrons have transitioned from their ground-state energy level to an excited energy state. Due to their large transition dipole moments, Rydberg atoms can strongly interact with incident RF signals, triggering electron transitions between resonant energy levels [4]. Capitalizing on these transitions, RAREs can capture the amplitude, frequency, phase, and polarization of RF signals with unparalleled precision. Consequently, RAREs have the potential to complement or even replace traditional RF receivers in the next-generation communications and sensing (C&S) systems [7]–[14].

RAREs offer two major advantages over classical receivers: extremely high sensitivity and a wide range of detectable frequency bands. Classical receivers, comprising metallic antennas and RF front-end circuitry, are fundamentally constrained by Johnson-Nyquist noise that arises from the random thermal motion of free electrons [15]. In contrast, the quantum process governing RAREs—electron transition between Rydberg states—is inherently immune to thermal noise. This immunity enables RAREs to achieve exceptional sensitivity to RF signals, potentially two orders of magnitude higher than that of traditional counterparts as demonstrated in [16], [17]. Additionally, conventional metallic antennas require physical dimensions comparable to the carrier wavelength to efficiently couple with incident RF signals. As a result, their detectable frequency ranges are intrinsically limited by their geometric size [18]. Conversely, RAREs circumvent this limitation entirely due to their atomic-scale Rydberg sensors, which eliminate wavelength-dependent antenna constraints while providing access to numerous energy levels. By utilizing electron transitions between these energy levels, a single RARE can simultaneously detect multiple distinct frequency bands, ranging from Megahertz (MHz) to Terahertz (THz), without any change of the hardware [7]. This unique capability underpins the development of integrated full-frequency wireless C&S platforms, unifying sub-6G, midband, millimeter wave (mmWave), and THz bands into a single receiver architecture. This paper exploits the second advantage of RAREs, their multi-band detection capability, to revolutionize wireless C&S systems.

Existing studies have experimentally validated the concurrent multi-band C&S capabilities of RAREs. The initial demonstration of dual-band communications was reported in [19], where two species of Rydberg alkali atoms—rubidium (Rb) and cesium (Cs)—each with distinct energy-level structures, were mixed in a single vapor cell. This configuration enabled the simultaneous detection of amplitude-modulated (AM) signals at 19.626 GHz and frequency-modulated (FM) signals at 20.644 GHz. Subsequent research in [20] proposed that leveraging the electron transitions between different energy levels within a single atom species, such as Cs, is sufficient to capture multiple frequency bands, a principle now widely adopted in multi-band RARE implementations. In particular, [21] reported the concurrent measurement of frequency bands at 1.72, 12.11, 27.42, 65.11, and 115.75 GHz. This was accomplished by utilizing *quantum heterodyne sensing* technology, which introduces external reference signals to assist signal detection, to excite electron transitions between energy levels, $56D_{5/2}$, $57P_{3/2}$, $54F_{7/2}$, $52F_{7/2}$, and $59P_{3/2}$. Further advances include chip-integrated RAREs for dual-band operation at 300 MHz and 24 GHz [22], and a cascaded orbital

The authors are with Department of Electrical and Electronic Engineering, The University of Hong Kong, Hong Kong (Emails: {mycui, qszeng, zhanwei, huangk} @eee.hku.hk). Corresponding authors: Q. Zeng; K. Huang.

angular-momentum transitions to enable coverage from 128 MHz to 0.61 THz [23]. Additionally, experiments conducted in [24] revealed the exclusive effect of multi-band RAREs. The effect indicates that the sensitivities of a RARE to different frequency bands can influence each other—an increase in sensitivity to one band might result in decreased sensitivity to other bands. Some studies have also explored the applications of multi-band RAREs. For example, authors in [25] applied multi-band RAREs to frequency-hopping communications. Their experiment, utilizing a hopping rate of 20000 hop/s, showcased a flexible frequency hop between carrier frequencies of 3.05 GHz and 15.29 GHz. Recently, an emerging study from the communication society, [26], applied multi-band RAREs to conduct angle-of-arrivals (AoAs) sensing at sub-6G and mmWave bands from a signal processing perspective.

However, the investigation of RAREs for multi-band C&S is still in its infancy. Currently, there is no interpretable model to mathematically characterize the working mechanisms of multi-band RAREs. Prior studies by the physics community [19]–[25] have predominantly emphasized experimental verifications without offering interpretable signal models. In the existing literature, only the work in [26] from the communication society introduces a signal model. However, this derivation directly adopts the conventional single-band RARE framework, which might be insufficient for accurately describing a realistic multi-band RARE. The absence of physics-compliant signal models leaves the multi-band RARE as a black box, hindering rigorous analysis of their quantum phenomena (e.g., the exclusive effect [24]) and performance optimization. To the best of our knowledge, establishing mathematical frameworks that accurately describe multi-band RAREs' dynamics remains an open challenge in the field. Addressing this challenge is crucial for fully unlocking the potential of multi-band RAREs in next-generation C&S systems.

To fill in this knowledge gap, this paper investigates the underlying mechanisms of multi-band RAREs and explores their performance limits in wireless C&S systems. We leverage multi-level electron transitions in Rydberg atoms to enable simultaneous multi-band signal reception, augmented by quantum heterodyne sensing to facilitate signal detection. Notably, the proposed multi-band RARE architecture fundamentally differs from conventional orthogonal frequency-division multiplexing (OFDM) systems [14]. In conventional OFDM systems, signals are confined to a single contiguous frequency block (e.g., a 100 MHz channel at 3.5 GHz in 5G New Radio standard [27]). In contrast, our multi-band RARE architecture supports concurrent operation across disjoint frequency bands, enabling simultaneous signal reception in spectrally distant regions (e.g., sub-6 GHz, mmWave, and THz bands). The key contributions and findings of our work are summarized as follows.

- **Mechanism of multi-band RAREs:** We developed a theoretical framework to characterize the operational mechanism of realistic multi-band RAREs. By solving the Lindblad master equation under steady-state conditions, we derive a closed-form expression for the quantum response of Rydberg atoms excited by multi-band RF signals. This solution rigorously quantifies the transfer function

of multi-band RAREs, revealing their dual role as *multi-band atomic mixers* and *multi-band atomic amplifiers*. Specifically, each wireless signal undergoes frequency down-conversion to the intermediate frequency (IF) via the transition frequency of its corresponding electron state coupling. The IF component is then amplified by a band-specific gain factor. Our analysis demonstrates that the sensitivity of a RARE to each frequency band is directly governed by this gain factor.

- **Sensitivity maximization of multi-band RAREs:** We establish an optimization framework to maximize the sensitivities of a RARE across all frequency bands by tuning the Rabi frequencies (electron transition strengths) of external reference signals in heterodyne sensing. This problem is inherently complex due to the mutual coupling among multi-band gain factors. To resolve this, we prove that each gain factor decomposes into a *global gain* term (common to all bands) and a *Rabi attention* term (band-specific). The global gain term remains consistent across all frequency bands as it depends solely on the sum-square of Rabi frequencies across all bands, referred to as the *Rabi sum-square*. Our findings reveal that the overall sensitivity of a RARE to all frequency bands is determined by this global gain. Therefore, the maximization of the overall sensitivity can be achieved by optimizing the Rabi sum-square rather than individual Rabi frequencies, for which the globally optimal solution is derived. The Rabi attention term characterizes the proportion of Rabi frequency at each band relative to those at all frequency bands. This term influences the allocation of overall sensitivity to each band, representing the unique attention mechanism of a multi-band RARE. These Rabi attentions can be either predetermined or optimized based on downstream C&S metrics.
- **C&S applications of multi-band RAREs:** We investigate the practical utility of multi-band RAREs in C&S systems, demonstrating their capability to support applications such as multi-heterogeneous-device communications and multi-granularity sensing. Performance is evaluated using two metrics: spectral efficiency (SE) for communications and normalized Cramér-Rao lower bound (CRLB) for sensing, both averaged across frequency bands. We give out the optimal design of Rabi attentions to maximize these multi-band C&S metrics. Numerical experiments validate the superiority of a multi-band RARE over the classic receivers and the existing single-band RARE.

The remainder of the paper is organized as follows. The mechanism of the multi-band RARE is mathematically interpreted in Section II. The maximal sensitivity of a multi-band RARE is analyzed in Section III. Section IV elaborates on the applications of multi-band RARE in C&S systems and the associated optimal Rabi attention design. Numerical experiments are conducted in Section V, and conclusions are drawn in Section VI.

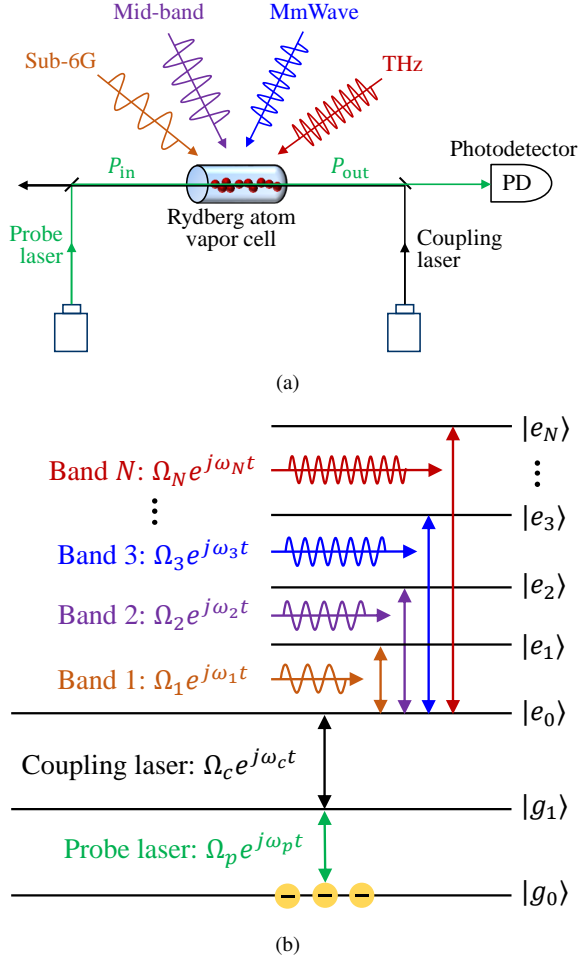


Figure 1. (a) The architecture of a multi-band RARE. (b) The multi-level electron transition for measuring multi-band signals.

II. MECHANISM OF MULTI-BAND RARE

Consider the multi-band RARE as illustrated in Fig. 1 (a). A single RARE is employed to simultaneously detect multi-band signals spanning from sub-6G to THz, offering diverse C&S services. This section delves into the underlying mechanisms of multi-band RAREs. We commence by modeling the incident multi-band signal. Subsequently, the electron transitions behavior of Rydberg atoms induced by multi-band signals is elucidated by solving the Lindblad master equation. Later, the multi-band heterodyne sensing technique is introduced for detecting multi-band signals, followed by discussions on baseband processing and the noise model.

A. Incident Multi-Band Signals

The incident multi-band signal consists of N distinct frequency bands, where the band spacings can extend up to tens of GHz. For the n -th frequency band, the incident RF signal is expressed as

$$E_{\text{RF},n}(t) = \text{Re}\{E_n(t)e^{j\omega_n t}\}, \quad (1)$$

where ω_n denotes the carrier frequency of band n and $E_n(t) \in \mathbb{C}$ the complex baseband signal. Both the transmitted modulation symbol in communication applications and the

target information in sensing applications can be embedded within $E_n(t)$, which will be elaborated in Section IV. The incident multi-band signal is thereby the superposition of $E_{\text{RF},n}(t)$, $\forall n \in \{1, \dots, N\}$, giving that

$$E_{\text{RF}}(t) = \sum_{n=1}^N E_{\text{RF},n}(t) = \sum_{n=1}^N \text{Re}\{E_n(t)e^{j\omega_n t}\}. \quad (2)$$

For classical receivers, detecting the signal $E_{\text{RF}}(t)$ necessitates multiple antennas and RF front-end circuits due to the largely separated frequency bands [28]. However, a single RARE is sufficient to capture $E_{\text{RF}}(t)$, as elaborated in the upcoming discussion.

B. Mechanism of Multi-Level Electron Transition

As illustrated in Fig. 1, a RARE utilizes the multi-level electron transitions of Rydberg atoms to interact with the multi-band signal, $E_{\text{RF}}(t)$. This interaction changes the quantum states of Rydberg atoms, resulting in variations in the absorption rate of the atomic vapor cell to an incoming laser. By propagating a probe laser through the vapor cell and then monitoring the output probe-laser power using a photodetector (PD), the quantum state can be readout, thereby enabling the detection of multi-band signals.

Specifically, alkali atoms, such as Rb and Cs, are stored in a glass vapor cell. A probe laser and a coupling laser propagate in opposite directions through this vapor cell to prepare Rydberg atoms. The probe laser excites electrons to jump from the ground state, denoted as $|g_0\rangle$, to a lowly excited state, denoted as $|g_1\rangle$. The coupling laser further triggers the electron transition from $|g_1\rangle$ to an initial Rydberg state, $|e_0\rangle$, thereby creating Rydberg atoms. These atoms interact with each frequency band of the incident RF signal, say band n , via the electron transition $|e_0\rangle \rightarrow |e_n\rangle$, $n \in \{1, 2, \dots, N\}$, respectively. As a result, the quantum response of each Rydberg atom is characterized by an $(N+3)$ -level quantum system, as depicted in Fig. 1(b). For ease of discussion, we define $\mu_{g_0g_1}$, $\mu_{g_1e_0}$, and μ_n , $\forall n \in \{1, \dots, N\}$ as the transition dipole moments associated with the electron transitions, $|g_0\rangle \rightarrow |g_1\rangle$, $|g_1\rangle \rightarrow |e_0\rangle$, and $|e_0\rangle \rightarrow |e_n\rangle$, $\forall n$, respectively. Similarly, we define $\omega_{g_0g_1}$, $\omega_{g_1e_0}$, and $\omega_{e_0e_n}$, $\forall n$ as the transition frequencies of these electron transitions. We suppose that the amplitude and frequency of probe laser (coupling laser) are fixed as E_p (E_c) and ω_p (ω_c), respectively. Based on these definitions, the Rabi frequency of each signal component, which quantifies the strength of the interaction between the signal and the electron transition, can be represented as [29]

$$\begin{cases} \Omega_p = \frac{\mu_{g_0g_1}}{\hbar} |E_p| \\ \Omega_c = \frac{\mu_{g_1e_0}}{\hbar} |E_c| \end{cases}, \quad (3)$$

for the probe and coupling lasers respectively, and as

$$\Omega_n = \frac{\mu_n}{\hbar} |E_n(t)|, \forall n \in \{1, 2, \dots, N\} \quad (4)$$

for the multi-band signals. Here, \hbar is the reduced Plank constant. In this work, we consider the resonant case for all electron transitions, meaning that $\omega_p = \omega_{g_0g_1}$, $\omega_c = \omega_{g_1e_0}$, and $\omega_n = \omega_{e_0e_n}$, $\forall n \in \{1, 2, \dots, N\}$.

To grasp the electron transition behavior in Fig. 1, we initially examine a dual-band system with $N = 2$ and subsequently extend our analysis to arbitrary multi-band systems. Specifically, the quantum system in Fig. 1(b) has five energy levels when $N = 2$. The Hamiltonian operator for this system is represented by a 5×5 Hermitian matrix

$$\mathbf{H} = \frac{\hbar}{2} \begin{bmatrix} 0 & \Omega_p & 0 & 0 & 0 \\ \Omega_p & 0 & \Omega_c & 0 & 0 \\ 0 & \Omega_c & 0 & \Omega_1 & \Omega_2 \\ 0 & 0 & \Omega_1 & 0 & 0 \\ 0 & 0 & \Omega_2 & 0 & 0 \end{bmatrix}, \quad (5)$$

which encompasses the Rabi frequencies of all external signals. Driven by this operator, the quantum state, denoted as a density matrix $\rho \in \mathbb{C}^{5 \times 5}$, evolves according to the Lindblad master equation [30]

$$\frac{\partial \rho}{\partial t} = \frac{j}{\hbar} [\rho, \mathbf{H}] + \mathcal{L}. \quad (6)$$

The operator \mathcal{L} characterizes the noncoherent relaxation of the system, which is given in (7). Here, $\gamma_{ij} = (\gamma_i + \gamma_j)$, where γ_i ($i = 2, 3, 4, 5$) refers to the decay rate of each energy level. In practice, the decay rate γ_2 is greater than γ_3 , γ_4 , and γ_5 by three orders of magnitude [30]. Thus, we can simplify (7) as

$$\mathcal{L} = -\frac{\gamma_2}{2} \begin{bmatrix} -2\rho_{22} & \rho_{12} & 0 & 0 & 0 \\ \rho_{21} & 2\rho_{22} & \rho_{23} & \rho_{24} & \rho_{25} \\ 0 & \rho_{32} & 0 & 0 & 0 \\ 0 & \rho_{42} & 0 & 0 & 0 \\ 0 & \rho_{52} & 0 & 0 & 0 \end{bmatrix}. \quad (8)$$

We are interested in the steady-state solution of the (2,1)-th entry of ρ , denoted as ρ_{12} , due to its direct correspondence with the probe laser to be measured. The following theorem provides the closed-form expression for ρ_{12} .

Theorem 1. *The steady-state solution of ρ_{12} to the Lindblad master equation in (6) is*

$$\rho_{12} = j \frac{\rho_0 (\Omega_1^2 + \Omega_2^2)}{(\Omega_1^2 + \Omega_2^2) + \Gamma^2}, \quad (9)$$

where $\rho_0 \triangleq \frac{\gamma_2 \Omega_p}{\gamma_2^2 + 2\Omega_p^2}$ and $\Gamma \triangleq \sqrt{\frac{2\Omega_p^2 (\Omega_c^2 + \Omega_p^2)}{\gamma_2^2 + 2\Omega_p^2}}$.

Proof: The expression in (9) is derived by imposing the steady-state condition $\frac{\partial \rho}{\partial t} = 0$ and solving the linear equations governed by the Lindblad master equation (6), which comprises 25 variables corresponding to the density matrix elements. For brevity, the full derivation is omitted here, though the complete solutions for all elements of ρ , including ρ_{12} , are rigorously validated and provided in Appendix A for reproducibility. \square

The coherence term ρ_{12} explicitly depends on the Rabi frequencies Ω_1 and Ω_2 of the dual-band signals, enabling the RARE to concurrently extract information from both frequency bands. Theorem 1 demonstrates that the derived ρ_{12} expression for the *dual-band* RARE generalizes prior *single-band* RARE formulations [30], [31], which is governed by

$$\rho_{12} = j \frac{\rho_0 \Omega_1^2}{\Omega_1^2 + \Gamma^2}. \quad (10)$$

Notably, setting $\Omega_2 = 0$ (or $\Omega_1 = 0$) in Theorem 1 recovers the single-band solution in (10), thereby validating the consistency of our generalized model.

Remark 1. (From dual-band to multi-band systems) *Theorem 1 indicates that the quantum state, ρ_{12} , is determined by the sum square of Rabi frequencies, $\Omega_1^2 + \Omega_2^2$. Extending this result to an arbitrary N -band system, the steady-state solution of the coherence term ρ_{12} generalizes to*

$$\rho_{12} = j \frac{\rho_0 \sum_{n=1}^N \Omega_n^2}{\sum_{n=1}^N \Omega_n^2 + \Gamma^2}, \quad (11)$$

where the dependence on $\sum_{n=1}^N \Omega_n^2$ reflects the collective contribution of all N frequency bands. This result is numerically validated in Section V-B.

Recall that a RARE readouts the quantum state by monitoring the probe laser. In practice, the imaginary part of ρ_{12} determines the absorption rate of the vapor cell to the probe laser. According to the adiabatic approximation, the power of probe laser coming out of the vapor cell is written as [30]

$$\begin{aligned} \mathcal{P}(\Omega) &= P_{\text{in}} \exp(-C_0 \text{Im}\{\rho_{12}\}) \\ &= P_{\text{in}} \exp\left(-\chi_0 \frac{\sum_{n=1}^N \Omega_n^2}{\sum_{n=1}^N \Omega_n^2 + \Gamma^2}\right), \end{aligned} \quad (12)$$

wherein $\Omega \triangleq [\Omega_1, \Omega_2, \dots, \Omega_N]^T$ stands for the Rabi frequency vector, and P_{in} denotes the input power of probe laser. The constants C_0 and χ_0 are defined as $C_0 \triangleq \frac{2N_0 \mu_{g0}^2 \epsilon_1 k_p L}{\epsilon_0 \hbar \Omega_p}$ and $\chi_0 \triangleq C_0 \rho_0$. Here, N_0 represents the total density of atoms, ϵ_0 the vacuum permittivity, L the length of vapor cell, and k_p the wavenumber of probe laser. Equations (2), (11), and (12) reveal the microwave-to-optical conversion process of a multi-band RARE, where the multi-band RF signals, $E_n(t)$, $\forall n$, are converted into the output laser power, $\mathcal{P}(\Omega)$. This process enables the co-detection of multiple frequency bands. For convenience in future use, we also give out the derivative of $\mathcal{P}(\Omega)$ with respect to (w.r.t.) Ω_n , $\forall n \in \{1, 2, \dots, N\}$:

$$\frac{\partial \mathcal{P}(\Omega)}{\partial \Omega_n} = \mathcal{P}(\Omega) \frac{2\chi_0 \Gamma^2 \Omega_n}{(\sum_{m=1}^N \Omega_m^2 + \Gamma^2)^2}. \quad (13)$$

$$\mathcal{L} = \begin{bmatrix} \gamma_2 \rho_{22} + \gamma_4 \rho_{44} + \gamma_5 \rho_{55} & -\frac{\gamma_2}{2} \rho_{12} & -\frac{\gamma_3}{2} \rho_{13} & -\frac{\gamma_4}{2} \rho_{14} & -\frac{\gamma_5}{2} \rho_{15} \\ -\frac{\gamma_2}{2} \rho_{21} & \gamma_3 \rho_{33} - \gamma_2 \rho_{22} & -\frac{\gamma_{23}}{2} \rho_{23} & -\frac{\gamma_{24}}{2} \rho_{24} & -\frac{\gamma_{25}}{2} \rho_{25} \\ -\frac{\gamma_3}{2} \rho_{31} & -\frac{\gamma_{23}}{2} \rho_{32} & -\gamma_3 \rho_{33} & -\frac{\gamma_{34}}{2} \rho_{34} & -\frac{\gamma_{35}}{2} \rho_{35} \\ -\frac{\gamma_4}{2} \rho_{41} & -\frac{\gamma_{24}}{2} \rho_{42} & -\frac{\gamma_{34}}{2} \rho_{43} & -\gamma_4 \rho_{44} & -\frac{\gamma_{45}}{2} \rho_{45} \\ -\frac{\gamma_5}{2} \rho_{51} & -\frac{\gamma_{25}}{2} \rho_{52} & -\frac{\gamma_{35}}{2} \rho_{53} & -\frac{\gamma_{45}}{2} \rho_{54} & -\gamma_5 \rho_{55} \end{bmatrix}. \quad (7)$$

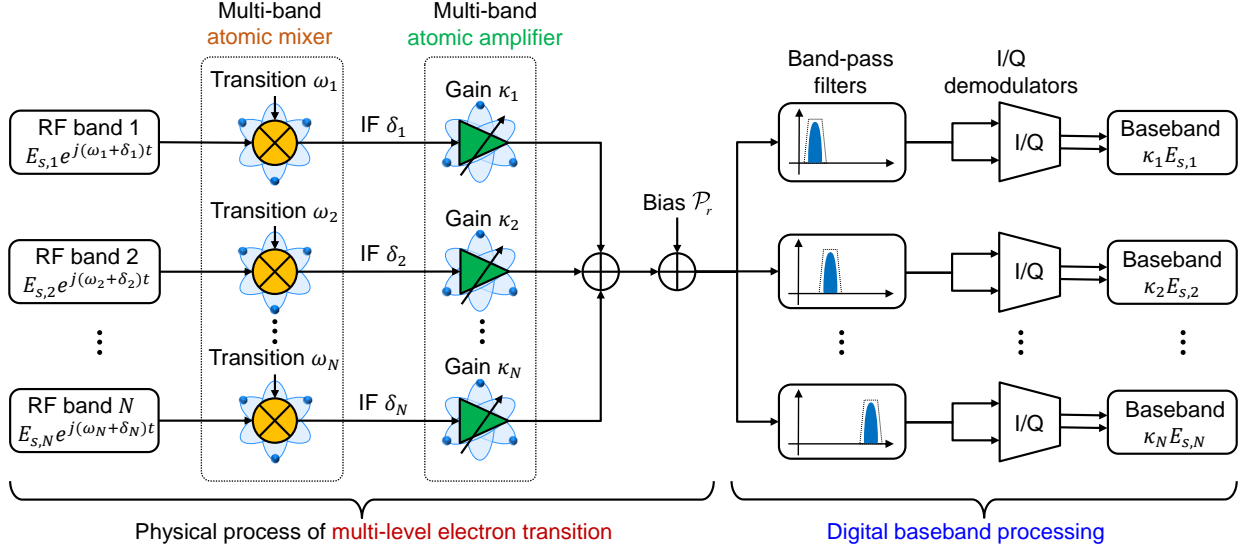


Figure 2. Equivalent signal transmission model of a multi-band RARE.

C. Mechanism of Multi-Band Heterodyne Sensing

Building on the derived multi-level electron transition model, we now elaborate the multi-band signal detection mechanism in RAREs. State-of-the-art multi-band RARE systems employ heterodyne sensing to recover wireless signals from the probe-laser power [21]. This technique utilizes external local oscillators (LOs), also known as reference sources, to generate reference signals that match the target wireless frequencies. For clarity, we designate the signals of interest as “data signals”, while the preconfigured LO-generated signals are termed “reference signals”.

To be specific, for the n -th band, we use $\text{Re}\{E_{r,n}e^{j\omega_n t}\}$ to represent the incident reference signal. Here, the complex baseband signal, $E_{r,n} \in \mathbb{C}$, is perfectly known to the RARE and can be freely adjusted by controlling the transmission power of the reference source. The incident data signal is denoted as $\text{Re}\{E_{s,n}e^{j(\omega_n + \delta_n)t}\}$, where the baseband component, $E_{s,n} \in \mathbb{C}$, carries the communication or sensing information of interest. The frequency offset δ_n characterizes the intermediate frequency (IF) pertaining to the n -th band, which is typically around 100kHz. Consequently, the overall incident RF signal, i.e., $E_{\text{RF},n}(t)$ in (1), become the superposition of the reference and data signals

$$E_{\text{RF},n}(t) = \text{Re}\left\{\underbrace{(E_{r,n} + E_{s,n}e^{j\delta_n t})}_{E_n(t)}e^{j\omega_n t}\right\}, \quad (14)$$

where $E_n(t)$ represents the composite baseband signal. Recalling the definition of Rabi frequency in (4), we can explicitly express the Rabi frequencies, $\Omega_{r,n}$, $\Omega_{s,n}$, and Ω_n of the reference, data, and overall signals as

$$\begin{cases} \Omega_{r,n} = \frac{\mu_n}{\hbar}|E_{r,n}| \\ \Omega_{s,n} = \frac{\mu_n}{\hbar}|E_{s,n}e^{j\delta_n t}| = \frac{\mu_n}{\hbar}|E_{s,n}| \\ \Omega_n = \frac{\mu_n}{\hbar}|E_n(t)| = |\Omega_{r,n} + \Omega_{s,n}e^{j(\delta_n t + \varphi_n)}| \end{cases}, \quad (15)$$

where $\varphi_n = \angle E_{s,n} - \angle E_{r,n}$ denotes the phase difference between $E_{s,n}$ and $E_{r,n}$. For convenience, we define the

Rabi frequency vectors of the reference signals, data signals, and overall signals as $\mathbf{\Omega}_r = [\Omega_{r,1}, \dots, \Omega_{r,N}]^T$, $\mathbf{\Omega}_s = [\Omega_{s,1}, \dots, \Omega_{s,N}]^T$, and $\mathbf{\Omega} = [\Omega_1, \dots, \Omega_N]^T$, respectively.

By substituting (15) into (12), the measured probe-laser power, which represents the transfer function of multi-band RAREs, is thereby obtained as

$$\begin{aligned} y(t) &= \mathcal{P}(\mathbf{\Omega}) \\ &= P_{\text{in}} \exp\left(-\frac{\chi_0 \sum_{n=1}^N |\Omega_{r,n} + \Omega_{s,n}e^{j(\delta_n t + \varphi_n)}|^2}{\sum_{n=1}^N |\Omega_{r,n} + \Omega_{s,n}e^{j(\delta_n t + \varphi_n)}|^2 + \Gamma^2}\right). \end{aligned} \quad (16)$$

In practice, the strength of the reference signal is orders of magnitude greater than that of the data signal due to the proximity of the reference source to the RARE. Henceforth, we have $E_{r,n} \gg E_{s,n}$ and $\Omega_{r,n} \gg \Omega_{s,n}, \forall n$. Under this strong-reference regime, the nonlinear transfer function in (16) can be linearized via a first-order Taylor expansion, as derived in (17). The resulting probe-laser power in (17) consists of three components: 1) a direct current (DC) bias, defined as $\mathcal{P}_r \triangleq \mathcal{P}(\mathbf{\Omega}_r)$, resulting from the strong reference signal; 2) a band-specific gain factor, defined as $\kappa_n \triangleq \frac{\partial \mathcal{P}(\mathbf{\Omega}_r)}{\partial \Omega_{r,n}} \frac{\mu_n}{\hbar}$, quantifying the RARE’s sensitivity for the n -th band; and 3) the modulated data signal, represented as $\text{Re}\{E_{s,n}e^{j(\delta_n t - \angle E_{r,n})}\}$, carrying the information payload. From (17), we can figure out the physical significance of a multi-band RARE.

Remark 2. (Physical significance of a multi-band RARE) A multi-band RARE operates as both a multi-band atomic mixer and a multi-band atomic amplifier, as illustrated in Fig. 2. The detection mechanism proceeds as follows:

- **Frequency mixing:** The data signal at each band ($\omega_n + \delta_n$) couples to the electron transition $|e_0\rangle \rightarrow |e_n\rangle$, inducing coherent down-conversion via the resonant frequency $\omega_{e_0 e_n} = \omega_n$. This generates an IF component at δ_n .
- **Amplification:** Each IF signal is amplified by the band-specific gain factor κ_n , determined by the RARE’s sensitivity to the n -th reference signal.

$$y(t) \approx \underbrace{\mathcal{P}(\Omega_r)}_{\text{DC bias}} + \sum_{n=1}^N \underbrace{\frac{\partial \mathcal{P}(\Omega_r)}{\partial \Omega_{r,n}} \frac{\mu_n}{\hbar}}_{\text{Gain for band } n} \underbrace{\text{Re}\{E_{s,n} e^{j(\delta_n t - \angle E_{r,n})}\}}_{\text{Data signal at band } n} \triangleq \mathcal{P}_r + \sum_{n=1}^N \kappa_n \text{Re}\{E_{s,n} e^{j(\delta_n t - \angle E_{r,n})}\} \quad (17)$$

- **Signal aggregation:** The amplified IF components from all bands superimpose in the probe-laser power $\mathcal{P}(\Omega)$, enabling simultaneous multi-band signal recovery.

D. Baseband Processing

After obtaining the probe-laser power from the PD, digital baseband processing is conducted to perform multi-band signal detection. To prevent inter-band interference, it is essential to make the IF components, $\text{Re}\{E_{s,n} e^{j(\delta_n t + \varphi_n)}\}$, mutually orthogonal. Specifically, we denote the occupied bandwidth of the n -th frequency band as B_n , with IFs ordered as $\delta_1 < \delta_2 < \dots < \delta_N$. Consequently, the minimum frequency separation between adjacent IFs, $\frac{\delta_{n+1} - \delta_n}{2\pi}$, should exceed $(B_n + B_{n+1})/2$ by an adequate safe margin. For instance, we can set $N = 3$, $\delta_1 = 2\pi \times 100$ kHz, $\delta_2 = 2\pi \times 200$ kHz, $\delta_3 = 2\pi \times 300$ kHz, and $B_1 = B_2 = B_3 = 80$ kHz. Under this orthogonal condition, the data signal at each frequency band can be independently captured using band-pass filters and I/Q demodulators, as shown in the right part of Fig. 2. Finally, the noiseless baseband signal originating from the n -th frequency band is obtained as

$$y_n = \kappa_n E_{s,n}, \forall n \in \{1, 2, \dots, N\}. \quad (18)$$

The outputs $\{y_n\}$ enable multi-band C&S applications, as detailed in Section IV.

E. Noise Characterization

In the final part of this section, we characterize the noise affecting the detected signal y_n . As discussed in [5], [16], the noise of a RARE comprises two primary components: extrinsic noise and intrinsic noise.

1) *Extrinsic noise:* The extrinsic noise originates predominantly from black-body radiation. This noise contaminates the incident data signals over the air, thus resulting in a noisy Rabi frequency

$$\begin{aligned} \Omega_n &= \frac{\mu_n}{\hbar} |E_n(t) + w_{E,n}(t)| \\ &= \frac{\mu_n}{\hbar} |E_{r,n} + E_{s,n} e^{j(\delta_n t + \varphi_n)} + w_{E,n}(t)|, \end{aligned} \quad (19)$$

where $w_{E,n}(t)$ represents the extrinsic noise in the free space. Due to the proximity of the reference source to the RARE, the strong-reference condition still holds, i.e., $|E_{r,n}| \gg |E_{s,n} e^{j(\delta_n t + \varphi_n)} + w_{E,n}(t)|$, allowing us to modify the linearization in (17) as

$$y(t) = \mathcal{P}_r + \sum_{n=1}^N \kappa_n \text{Re}\{E_{s,n} e^{j(\delta_n t - \angle E_{r,n})} + w_{E,n}(t)\}.$$

Note that the noise $w_{E,n}(t)$ is amplified by the gain factor κ_n as well. After passing through the band-pass filter of

bandwidth B_n and the I/Q demodulator, the baseband signal polluted by black-body radiation is thus

$$y_n = \kappa_n E_n + w_{E,n}. \quad (20)$$

According to [13], the power of $w_{E,n}$ is formulated as

$$\sigma_{E,n}^2 = \kappa_n^2 B_n \frac{c \hbar \omega_n \rho_v A_e}{12(\exp(\hbar \omega_n / k_B T) - 1)} \triangleq \kappa_n^2 B_n C_1. \quad (21)$$

where $\rho_v \triangleq \frac{2\omega_n^2}{\pi c^3}$ represents the volumetric and spectral density of modes, c the speed of light, A_e the effective area of the vapor cell, and T the room temperature.

2) *Intrinsic noise:* The intrinsic noise, $w_{I,n}$, is dominated by the photon shot noise (PSN) of the PD, scaling with the DC bias of probe-laser power, \mathcal{P}_r . The equivalent noise power for band n across bandwidth B_n is given by

$$\sigma_{I,n}^2 = \mathcal{P}_r B_n \frac{\hbar \omega_p}{\eta R} \triangleq \mathcal{P}_r B_n C_2, \quad (22)$$

where η denotes the quantum efficiency of PD and R the load resistance of PD. This PSN can be directly added onto the measured probe-laser power in (17).

Based on these discussions, the noisy baseband signal is recast as

$$y_n = \kappa_n E_n + w_{E,n} + w_{I,n} = \kappa_n E_n + w_n. \quad (23)$$

Here, the total noise, w_n is modeled as an additive Gaussian white noise following $w_n \sim \mathcal{CN}(0, \sigma_n^2)$ with variance

$$\sigma_n^2 = \sigma_{E,n}^2 + \sigma_{I,n}^2 = \kappa_n^2 B_n C_1 + \mathcal{P}_r B_n C_2. \quad (24)$$

III. MAXIMAL SENSITIVITY OF MULTI-BAND RARES

In this section, we maximize the sensitivity of a multi-band RARE by optimizing the multi-band atomic amplifier through the manipulation of the Rabi frequencies of reference signals. The explicit expression of the sensitivity is derived and analyzed, followed by quantifying the optimal Rabi frequencies.

A. Sensitivity Analysis for Multi-Band RARES

We utilize the Signal-to-Noise Ratio (SNR) of the baseband signal, y_n , to characterize the sensitivity of a multi-band RARE. For the n -th band, the SNR is given by

$$\text{SNR}_n = \frac{\kappa_n^2 |E_{s,n}|^2}{\kappa_n^2 B_n C_1 + \mathcal{P}_r B_n C_2} = \frac{|E_{s,n}|^2}{B_n C_1 + \frac{\mathcal{P}_r}{\kappa_n^2} B_n C_2}. \quad (25)$$

It is observed that SNR_n is monotonically increasing w.r.t. the parameter $\frac{\kappa_n^2}{\mathcal{P}_r}$. Note that both $\kappa_n = \frac{\partial \mathcal{P}(\Omega_r)}{\partial \Omega_{r,n}} \frac{\mu_n}{\hbar}$ and $\mathcal{P}_r = \mathcal{P}(\Omega_r)$ are affected by the Rabi frequency vector Ω_r of reference signals. Therefore, the sensitivity of RARE can be maximized by appropriately configuring the values

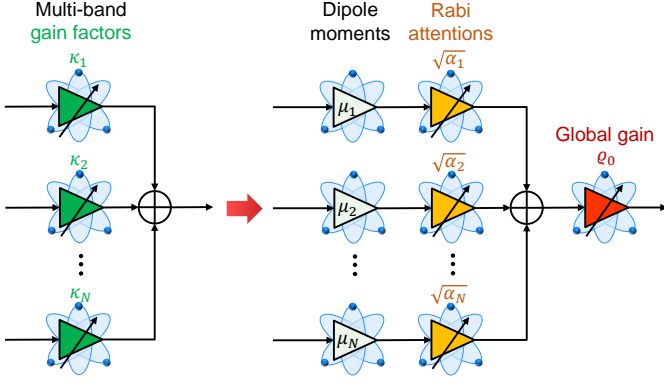


Figure 3. Decoupling of the multi-band atomic amplifier.

of Ω_r through the transmission power control at the reference sources. Unfortunately, the multi-band gain factors, $\{\kappa_1, \kappa_2, \dots, \kappa_N\}$, of the multi-band atomic amplifier are coupled with each other due to their intricate dependence on all Rabi frequencies, as shown in (12) and (13). This coupling makes the maximization of SNR_n nonconvex and challenging. To address this issue, we propose a method to decouple the gain κ_n from the joint dependence on Ω_r , enabling tractable optimization.

1) *Decoupling of the gain factor κ_n* : The concepts of *Rabi sum-square* and *Rabi attentions* are introduced to decouple the gain factor κ_n .

Definition 1. (Rabi sum-square and Rabi attentions) We define the *Rabi sum-square* as the sum square of the Rabi frequencies of the reference signals, denoted as

$$\mathcal{A} \triangleq \sum_{n=1}^N \Omega_{r,n}^2. \quad (26)$$

Additionally, we introduce the variables, referred to as the *Rabi attention*, as

$$\alpha_n \triangleq \frac{\Omega_{r,n}^2}{\sum_{m=1}^N \Omega_{r,m}^2}, \forall n \quad (27)$$

to characterize the ratio of $\Omega_{r,n}^2$ to the *Rabi sum-square* \mathcal{A} . The sum of all Rabi attentions equals 1 as $\sum_{n=1}^N \alpha_n = 1$.

One can observe that the optimization of the Rabi frequencies $[\Omega_{r,1}, \Omega_{r,2}, \dots, \Omega_{r,N}]$ is equivalent to the optimization of the Rabi sum-square and all Rabi attentions. This is attributed to the one-to-one mapping

$$\Omega_{r,n} = \sqrt{\mathcal{A}\alpha_n}, \forall n. \quad (28)$$

Utilizing this equivalence, the DC bias, \mathcal{P}_r , can be reformulated as a function of the Rabi sum-square:

$$\mathcal{P}_r = \mathcal{P}(\Omega_r) = P_{\text{in}} \exp\left(-\frac{\chi_0 \mathcal{A}}{\mathcal{A} + \Gamma^2}\right). \quad (29)$$

Moreover, the gain factor, κ_n , for band n can be recast as

$$\begin{aligned} \kappa_n &= \mathcal{P}_r \frac{2\chi_0 \Gamma^2 \Omega_{r,n}}{(\sum_{m=1}^N \Omega_{r,m}^2 + \Gamma^2)^2} \frac{\mu_n}{\hbar} = \mathcal{P}_r \frac{2\chi_0 \Gamma^2 \sqrt{\mathcal{A}\alpha_n}}{(\mathcal{A} + \Gamma^2)^2} \frac{\mu_n}{\hbar} \\ &= \frac{2\chi_0 \Gamma^2}{\hbar} \mathcal{P}_r \frac{\sqrt{\mathcal{A}}}{(\mathcal{A} + \Gamma^2)^2} \sqrt{\alpha_n} \mu_n \triangleq \varrho_0 \sqrt{\alpha_n} \mu_n, \end{aligned} \quad (30)$$

where

$$\varrho_0 \triangleq \frac{2\chi_0 \Gamma^2}{\hbar} \mathcal{P}_r \frac{\sqrt{\mathcal{A}}}{(\mathcal{A} + \Gamma^2)^2}. \quad (31)$$

The relationship in (30) reveals that the gain factor for band n is composed of three parts: the transition dipole moment μ_n , the parameter ϱ_0 termed as the *global gain*, and the Rabi attention $\sqrt{\alpha_n}$ ¹. This structure allows for the decoupling of the multi-band atomic amplifier in Fig. 3, which is elaborated in Remark 3.

Remark 3. (Decoupled multi-band atomic amplifier)

- **Global gain:** The global gain, ϱ_0 , depends solely on the *Rabi sum-square*, \mathcal{A} , which remains consistent across all frequency bands. This parameter determines the overall amplification gain, or equivalently the overall sensitivity, of the RARE to all frequency bands. Furthermore, the *Rabi sum-square* \mathcal{A} and Rabi attentions $\{\sqrt{\alpha_n}\}$ are independent variables, enabling decoupled optimization of the global gain and Rabi attentions.
- **Rabi attention:** The Rabi attentions, $\sqrt{\alpha_n}, \forall n$, characterize how the RARE allocates its overall sensitivity to different frequency bands. This attention mechanism is a distinctive feature of the multi-band RARE introduced by the multi-level electron transition process. Fixing the value of Rabi sum-square and increasing the proportion of $\Omega_{r,n}^2$ in the Rabi sum-square can enhance $\sqrt{\alpha_n}$, prioritizing sensitivity to the n -th band while proportionally reducing attention to others. This intrinsic tradeoff elucidates the experimentally observed exclusive effect of multi-band RAREs [24].
- **Transition dipole moment:** The transition dipole moments, $\mu_n, \forall n$, are constants determined by the Rydberg atoms' inherent response to each frequency band. These parameters remain fixed, reflecting the fundamental atomic properties rather than tunable operational settings.

As a result, the decoupling of multi-band atomic amplifiers allows us to *independently* optimize the global gain, ϱ_0 , and the Rabi attentions, $\sqrt{\alpha_n}$. This will significantly simplify the sensitivity maximization problem.

2) *SNR analysis*: Following the decoupled κ_n in (30), the SNR at band n is reformulated as

$$\text{SNR}_n = \frac{\alpha_n \mu_n^2 |E_{s,n}|^2}{\alpha_n \mu_n^2 B_n C_1 + \frac{\mathcal{P}_r}{\varrho_0^2} B_n C_2}. \quad (32)$$

Several insights can be drawn from (32). Firstly, the SNR is monotonically increasing w.r.t. the global gain normalized by the DC bias, $\frac{\varrho_0^2}{\mathcal{P}_r}$. The normalization arises from the PSN, that is linearly related to \mathcal{P}_r . Similar to the discussion in Remark 3, the normalized global gain, $\frac{\varrho_0^2}{\mathcal{P}_r}$, serves as a global parameter dependent only on the Rabi sum-square. Increasing its value allows for a uniform enhancement of the SNRs across all frequency bands. Therefore, the maximization of all $\text{SNR}_n, \forall n$ is achieved only if $\frac{\varrho_0^2}{\mathcal{P}_r}$ is maximized. Secondly, the

¹Without causing confusion, we will term both α_n and $\sqrt{\alpha_n}$ as the “Rabi attention” in subsequent discussions.

Rabi attentions, $\alpha_n, \forall n$, dictate the RARE's emphasis on each frequency band. By increasing α_n , the RARE can amplify the signal, $E_{s,n}$, with a larger gain. However, this also results in an increase in the extrinsic noise, $\sigma_{E,n}^2$, within the same band.

B. Optimal Rabi Sum-square for Sensitivity Maximization

This subsection derives the optimal Rabi sum-square $\mathcal{A} = \sum_{n=1}^N \Omega_{r,n}^2$ to maximize the normalized global gain $\frac{\varrho_0^2}{\mathcal{P}_r}$, thereby achieving maximal sensitivity across all frequency bands. Notably, the optimization of the Rabi attentions $\{\alpha_n\}$ is contingent on application-specific performance metrics for C&S, which are detailed in Section IV. To be specific, the sensitivity maximization problem is formulated as

$$\max_{\mathcal{A} > 0} \frac{\varrho_0^2}{\mathcal{P}_r}, \quad (33)$$

where

$$\frac{\varrho_0^2}{\mathcal{P}_r} = \frac{4\chi_0^2 \Gamma^4 P_{\text{in}}}{\hbar^2} \exp\left(-\frac{\chi_0 \mathcal{A}}{\mathcal{A} + \Gamma^2}\right) \frac{\mathcal{A}}{(\mathcal{A} + \Gamma^2)^4}. \quad (34)$$

The objective function in (34) comprises a constant, an exponential decay term, and a rational function of \mathcal{A} . Theorem 2 provides the closed-form global optimum for (33), which governs the fundamental sensitivity limits of the multi-band RARE.

Theorem 2. *The optimal \mathcal{A} that maximizes $\frac{\varrho_0^2}{\mathcal{P}_r}$ is*

$$\mathcal{A}^* = \frac{\chi_0 + 4 - \sqrt{\chi_0^2 + 4\chi_0 + 16}}{\chi_0 - 4 + \sqrt{\chi_0^2 + 4\chi_0 + 16}} \Gamma^2. \quad (35)$$

Proof: (See Appendix B). \square

The function $\frac{\varrho_0^2}{\mathcal{P}_r}$ is monotonically increasing for $\mathcal{A} < \mathcal{A}^*$ and monotonically decreasing for $\mathcal{A} > \mathcal{A}^*$. Utilizing Theorem 2, the normalized global gain $(\frac{\varrho_0}{\mathcal{P}_r})^*$, that maximizes sensitivity is acquired. By substituting \mathcal{A}^* into (29) and (31), we can also obtain the corresponding DC bias and global gain, denoted as \mathcal{P}_r^* and ϱ_0^* respectively. Furthermore, Theorem 2 reveals that for a multi-band RARE, regardless the number of frequency bands considered, the sum square of the multi-band Rabi frequencies of the reference signals, $\mathcal{A} = \sum_{n=1}^N \Omega_{r,n}^2$, must be \mathcal{A}^* . Since $\Omega_{n,r} = \frac{\mu_n}{\hbar} |E_{r,n}|$ is proportional to the incident electric field, this optimal condition implies a fixed weighted sum of received reference-signal powers:

$$\sum_{n=1}^N \frac{\mu_n^2}{\hbar^2} |E_{r,n}|^2 = \text{constant}. \quad (36)$$

Nevertheless, we can still control the proportion of Rabi frequencies $\Omega_{r,n}^2$ to flexibly manipulate the Rabi attentions, thereby further improving the C&S performances.

IV. APPLICATIONS OF MULTI-BAND RARES

In this section, we apply the multi-band RARE to C&S scenarios. We systematically derive the optimal Rabi attention factors $\{\alpha_n\}$ for each operational regime, establishing performance limits for concurrent multi-band detection.

A. Multi-Band Communications

1) *Overview of multi-band communication systems:* We first consider a multi-band communication system where a single RARE concurrently demodulates quadrature amplitude modulation (QAM) symbols from N heterogeneous transmitters operating at distinct frequency bands. Let $s_n \in \mathbb{S}_n$ denote the transmitted QAM symbol from the n -th device, normalized such that $\mathbb{E}[|s_n|^2] = 1$. Leveraging the multi-band RARE framework and the optimal total squared Rabi frequencies \mathcal{A}^* derived in Section III-B, the received signal at band n is

$$y_n = \kappa_n E_{s,n} + w_n = \varrho_0^* \sqrt{\alpha_n} \mu_n h_n \sqrt{P_{\text{tx},n}} s_n + w_n, \quad (37)$$

where $h_n \in \mathbb{C}$ is the flat-fading channel coefficient (assumed known via channel estimation), $\sqrt{P_{\text{tx},n}}$ is the transmit power at the n -th band, and $w_n \sim \mathcal{CN}(0, \sigma_n^2)$ represents additive noise with variance $\sigma_n^2 = \alpha_n \mu_n^2 \varrho_0^{*2} B_n C_1 + \mathcal{P}_r^* B_n C_2$. The multi-path effect is neglected due to the narrow bandwidth B_n of each band. The multi-band symbols $s_n, \forall n$ are recovered through the maximum-likelihood (ML) detector:

$$\hat{s}_n = \arg \min_{s_n \in \mathbb{S}_n} \|y_n - \varrho_0^* \sqrt{\alpha_n} \mu_n h_n \sqrt{P_{\text{tx},n}} s_n\|^2, \forall n, \quad (38)$$

where \mathbb{S}_n denotes the QAM constellation set.

2) *Optimal Rabi attentions for maximizing spectrum efficiency:* The spectrum efficiency is adopted as the performance metric of this multi-band communication system

$$\begin{aligned} \mathcal{C} &= \frac{\sum_{n=1}^N B_n \log_2(1 + \text{SNR}_n)}{\sum_{n=1}^N B_n} \\ &= \sum_{n=1}^N \gamma_n \log_2 \left(1 + \frac{\alpha_n \mu_n^2 \varrho_0^{*2} |h_n|^2 P_{\text{tx},n}}{\alpha_n \mu_n^2 \varrho_0^{*2} B_n C_1 + \mathcal{P}_r^* B_n C_2} \right), \end{aligned} \quad (39)$$

where $\gamma_n \triangleq \frac{B_n}{\sum_{m=1}^N B_m}$ denotes the proportion of bandwidth. For ease of discussion, the transmission power $P_{\text{tx},n}$ and bandwidth B_n are assumed to be fixed. We aim at maximizing spectrum efficiency \mathcal{C} by optimizing the Rabi attentions, $\{\alpha_n\}$, under the constraints $\sum_{n=1}^N \alpha_n = 1$ and $\alpha_n \geq 0, \forall n$. Let $\beta_n \triangleq \frac{|h_n|^2 P_{\text{tx},n}}{B_n C_1}$ and $\epsilon_n \triangleq \frac{\mathcal{P}_r^* C_2}{\mu_n^2 \varrho_0^{*2} C_1}$, simplifying the problem to:

$$\max_{\{\alpha_n\}_{n=1}^N} \sum_{n=1}^N \gamma_n \log_2 \left(1 + \frac{\beta_n \alpha_n}{\alpha_n + \epsilon_n} \right), \quad (40)$$

$$\text{s.t.} \quad \sum_{n=1}^N \alpha_n = 1, \quad (40a)$$

$$\alpha_n \geq 0, \forall n. \quad (40b)$$

To obtain the global optimal solution for Rabi attentions, the concavity of problem (40) is proved as follows: 1) *Constraints:* The constraints $\sum_{n=1}^N \alpha_n = 1$ and $\alpha_n \geq 0$ are clearly convex. 2) *Objective function:* The second derivative of \mathcal{C} w.r.t. α_n is

$$\frac{\partial^2 \mathcal{C}}{\partial \alpha_n^2} = -\log_2 \frac{\gamma_n \beta_n \epsilon_n (2(1 + \beta_n) \alpha_n + (2 + \beta_n) \epsilon_n)}{(\alpha_n + \epsilon_n)^2 ((1 + \beta_n) \alpha_n + \epsilon_n)^2} < 0, \quad (41)$$

and $\frac{\partial^2 \mathcal{C}}{\partial \alpha_n \partial \alpha_m} = 0, \forall n \neq m$, such that the Hessian matrix is diagonal with negative entries, confirming concavity. Therefore, the global optimal Rabi attentions can be attained by solving

Karush-Kuhn-Tucker (KKT) conditions [32], as presented in Theorem 3.

Theorem 3. *The optimal Rabi attentions, α_n , $\forall n \in \{1, 2, \dots, N\}$, that solve problem (40) satisfy*

$$\alpha_n^* = \left(\frac{-(2+\beta_n)\epsilon_n + \sqrt{\beta_n^2\epsilon_n^2 + 4\nu^*\gamma_n\beta_n(1+\beta_n)\epsilon_n}}{2(1+\beta_n)} \right)^+, \quad (42)$$

where $(x)^+ \triangleq \max(0, x)$, and the non-negative Lagrange multiplier ν^* is properly selected to ensure $\sum_{n=1}^N \alpha_n^* = 1$.

Proof: (See Appendix C). \square

Combining Theorem 2 and Theorem 3 yields the optimal design of Rabi frequencies of the reference signals: $\Omega_{r,n}^* = \sqrt{\mathcal{A}^* \alpha_n^*}$, where \mathcal{A}^* (Theorem 2) ensures maximal global sensitivity, and α_n^* (Theorem 3) optimizes band-specific spectrum efficiency. This joint optimization enables the multi-band RARE to achieve maximum spectrum efficiency in concurrent multi-band communication.

It needs to be emphasized the metric of spectrum efficiency is just one possible criterion for multi-band RAREs. Many other metrics could also be considered, such as energy efficiency, user fairness, and secure communication rate. These metrics will result in different optimal Rabi attentions, while the optimal Rabi sum-square can be kept as (35) because its design is independent of the specific metrics.

B. Multi-Band Sensing

1) *Overview of multi-band sensing systems:* Multi-band RARE can enable high-precision wireless sensing by exploiting the frequency-dependent phase sensitivity of RF signals. As the operating frequency ω increases, a minute target displacement d will induce a significant phase shift $\frac{\omega d}{c}$, enhancing sensing granularity. By simultaneously detecting N frequency bands, multi-band RAREs achieve multi-scale sensing from coarse (e.g., hand tracking) to fine (e.g., finger tracking) resolutions.

Consider the incident RF signal $\text{Re}\{E_{s,n}e^{j(\omega_n+\delta_n)t}\}$ used for sensing the n -th target. The sensing target has undergone a slight displacement, d_n , which introduces an additional phase, $\frac{(\omega_n+\delta_n)d_n}{c}$, to the sensing signal, $E_{s,n}$. Consequently, the received baseband signal at the RARE is expressed as

$$\begin{aligned} y_n &= \kappa_n E_{s,n} e^{j\frac{(\omega_n+\delta_n)d_n}{c}} + w_n \stackrel{(a)}{\approx} \kappa_n E_{s,n} e^{j\frac{\omega_n d_n}{c}} + w_n \\ &= \varrho_0^* \sqrt{\alpha_n \mu_n} E_{s,n} e^{j\frac{\omega_n d_n}{c}} + w_n, \end{aligned} \quad (43)$$

where the approximation (a) holds because $\omega_n \gg \delta_n$. To avoid phase ambiguity, displacements are constrained to $d_n \in \left[-\frac{\pi c}{\omega_n}, \frac{\pi c}{\omega_n}\right]$ [8], [10]. Our objective is to recover all displacements, $\{d_1, d_2, \dots, d_N\}$, from the received N -band signals, $\{y_1, y_2, \dots, y_N\}$. To this end, we use the ML detection method to estimate d_n as

$$\hat{d}_n = \frac{c}{\omega_n} \angle \left(\frac{y_n}{\varrho_0^* \sqrt{\alpha_n \mu_n} E_{s,n}} \right), \forall n. \quad (44)$$

The sensing accuracy of d_n can be assessed using the Cramer-Rao Lower Bound (CRLB):

$$\begin{aligned} \text{CRLB}(d_n) &= \frac{c^2}{\omega_n^2} \frac{1}{2\text{SNR}_n} = \frac{c^2 \alpha_n \mu_n^2 \varrho_0^{*2} B_n C_1 + c^2 \mathcal{P}_r B_n C_2}{2\omega_n^2 \alpha_n \mu_n^2 \varrho_0^{*2} |E_{s,n}|^2} \\ &= \frac{c^2 B_n C_1}{2\omega_n^2 |E_{s,n}|^2} + \frac{c^2 \mathcal{P}_r B_n C_2}{2\omega_n^2 \alpha_n \mu_n^2 \varrho_0^{*2} |E_{s,n}|^2}. \end{aligned} \quad (45)$$

2) Optimal Rabi attentions for minimizing sensing error:

To eliminate the discrepancies of CRLBs caused by the distinct feasible ranges of d_n , i.e., $d_n \in \left[-\frac{\pi c}{\omega_n}, \frac{\pi c}{\omega_n}\right]$, we use $\mathbb{E}[|d_n|^2]$ to normalize the CRLB. Assuming d_n a uniform distribution, $d_n \sim \mathcal{U}\left[-\frac{\pi c}{\omega_n}, \frac{\pi c}{\omega_n}\right]$, we normalize the CRLB by $\mathbb{E}[|d_n|^2] = \frac{\pi^2 c^2}{3\omega_n^2}$, yielding the normalized CRLB (NCRLB):

$$\text{NCRLB}(d_n) = \frac{3B_n C_1}{2\pi^2 |E_{s,n}|^2} + \frac{3\mathcal{P}_r B_n C_2}{2\pi^2 \alpha_n \mu_n^2 \varrho_0^{*2} |E_{s,n}|^2}. \quad (46)$$

The sum of all normalized CRLBs is adopted as a performance metric to evaluate the overall sensing error, which is minimized by optimizing the Rabi attentions. The notation $\xi_n \triangleq \frac{3\mathcal{P}_r B_n C_2}{2\pi^2 \mu_n^2 \varrho_0^{*2} |E_{s,n}|^2}$ is introduced to simplify the expression of the formulated problem as

$$\min_{\{\alpha_n\}_{n=1}^N} \sum_{n=1}^N \frac{\xi_n}{\alpha_n}, \quad (47)$$

$$\text{s.t.} \quad \sum_{n=1}^N \alpha_n = 1, \quad (47a)$$

$$\alpha_n \geq 0, \forall n. \quad (47b)$$

The term $\frac{3B_n C_1}{2\pi^2 |E_{s,n}|^2}$ in $\text{NCRLB}(d_n)$ is omitted in problem (47) as it is irrelevant to α_n . This optimization problem is shown to be convex, and its global optimal solution can be readily derived by solving KKT conditions as

$$\alpha_n^* = \frac{\sqrt{\xi_n}}{\sum_{m=1}^N \sqrt{\xi_m}}. \quad (48)$$

As a result, by configuring the Rabi frequencies as $\Omega_{r,n}^* = \sqrt{\mathcal{A}^* \alpha_n^*}$ using the optimal Rabi sum-square in Theorem 2 and the optimal Rabi attentions in (48), the maximal sensing accuracy averaged over multiple frequency bands is achieved.

V. NUMERICAL EXPERIMENTS

In this section, we present numerical experiments to verify the effectiveness of multi-band RARE.

A. Experimental Setup

The default experimental settings for the RARE are as follows unless specified otherwise. We consider a dual-band wireless system with $N = 2$, where sub-6G and mmWave signals are detected by a single RARE. Cs atoms are stored in a vapor cell with a length of $L = 2$ cm and an effective area of $A_e = 1$ cm², which has an atomic density of $N_0 = 4.89 \times 10^{10}$ cm⁻³. The probe laser having a wavelength of 852.94 nm and an input power of 120 μ W excites the atoms from the ground state $|g_0\rangle = 6S_{1/2}$ to the lowly excited state $|g_1\rangle = 6P_{3/2}$. The coupling laser, with a wavelength

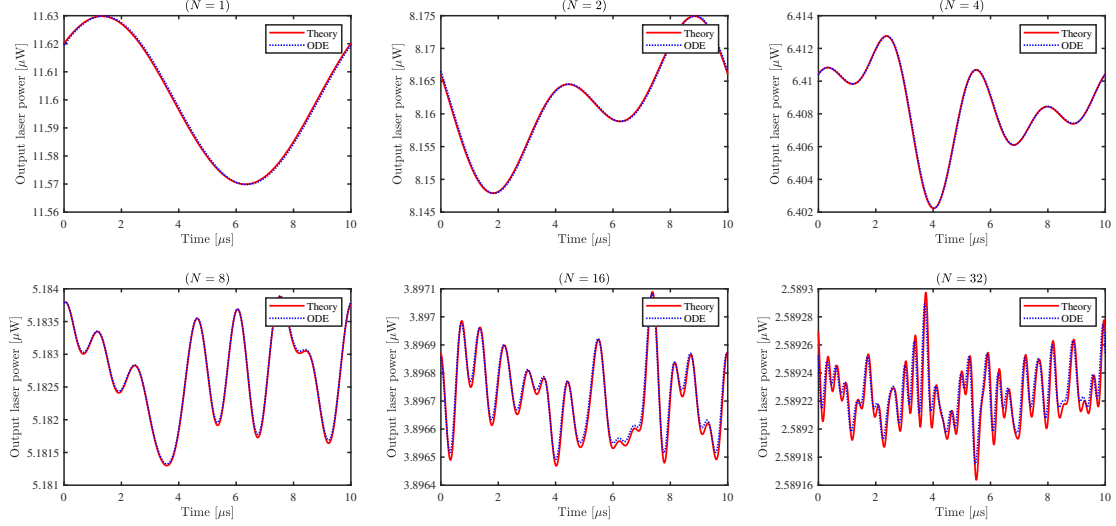


Figure 4. Waveforms of multi-band RAREs for $N = 1, 2, 4, 8, 16, 32$.

of 509.49 nm and a power of 17 mW, further triggers the atoms from $6P_{3/2}$ to the initial Rydberg state $|e_0\rangle = 60D_{5/2}$. The Rabi frequencies of the probe and coupling lasers are fixed as $2\pi \times 5.7$ MHz and $2\pi \times 0.97$ MHz, respectively. The two final Rydberg states are configured as $|e_1\rangle = 61P_{3/2}$, and $|e_2\rangle = 62P_{3/2}$. The electron transition $61P_{3/2} \rightarrow 62P_{3/2}$ resonates with the sub-6G signal operating at $\omega_{e_0e_1} = 2\pi \times 3.212$ GHz and the transition $61P_{3/2} \rightarrow 63P_{3/2}$ resonates with the mmWave signal operating at $\omega_{e_0e_2} = 2\pi \times 30.628$ GHz. The corresponding transition dipole moments are calculated as $\mu_{g_0g_1} = 2.586qa_0$, $\mu_{g_1e_0} = 0.013qa_0$, $\mu_1 = 2410qa_0$, and $\mu_2 = 736.452qa_0$, respectively, where $q = 1.602 \times 10^{-19}$ C denotes the unit charge and $a_0 = 52.9$ pm the Bohr radius [33]. The decay rate γ_2 is $2\pi \times 5.2$ MHz. The load resistance and quantum efficiency of PD are set as $R = 50$ Ohm and $\eta = 0.8$. Using these parameters, the optimal Rabi sum-square is calculated as $\sqrt{\mathcal{A}^*} = 2\pi \times 0.586$ MHz.

Furthermore, The configurations for the wireless signals are as follows. The frequencies of reference signals are tuned resonant with the electron transition frequencies, $\omega_1 = \omega_{e_0e_1} = 2\pi \times 3.212$ GHz and $\omega_2 = \omega_{e_0e_2} = 2\pi \times 30.628$ GHz. The IFs and occupied bandwidths of the dual-band signals are set as $\delta_1 = 2\pi \times 100$ kHz, $B_1 = 80$ kHz and $\delta_2 = 2\pi \times 200$ kHz, $B_2 = 80$ kHz. The transmission power of the two wireless data sources are configured as 20 dBm. The wireless channel fading is assumed to be -90 dB.

For comparison, two classic receivers working at $\omega_1 = 2\pi \times 3.212$ GHz and $\omega_2 = 2\pi \times 30.628$ GHz are deployed in the same wireless environment to detect the dual-band signal, which serve as the performance benchmarks. They are denoted as “CR1” for the sub-6G band and “CR2” for the mmWave band. Each of them is equipped with a single half-wavelength dipole antenna and a front-end circuit dedicated for each band. Their specific configurations are the same as the existing literature [16]. For example, the antenna gains and low-noise-amplifier (LNA) gains are set as 2.1 dB and 30 dB,

and the equivalent LNA noise temperature is 100 Kelvin.

B. Validation of Signal Transmission Model

To validate the effectiveness of our derived signal model, we present Fig. 4 to illustrate the alignment of waveforms between the signal model acquired in (17), labeled as “Theory”, and the exact solution, labeled as “ODE”. Here, the exact solution is numerically computed by using the ordinary differential equation (ODE) solver, (e.g., the fourth-order Runge-Kutta method), to address the Lindblad master equation given in (6). The number of frequency bands are set as $N = \{1, 2, 4, 8, 16, 32\}$. A time window of 10 μ s is selected to observe the waveforms, during which the amplitude of wireless signals for each band remains constant. The Rabi frequencies of reference signals are fixed as $\Omega_{l,n} = 2\pi \times 1$ MHz, $\forall n$, while the Rabi frequencies of data signals are randomly generated from the distribution $\Omega_{s,n} \sim 2\pi \times \mathcal{U}(0 \text{ kHz}, 1 \text{ kHz})$. Thereby, the strong reference signal condition, $|\Omega_{r,n}| \gg |\Omega_{s,n}|, \forall n$, is satisfied. The IFs for each frequency band are selected as $\delta_n/2\pi = 100n$ kHz, $\forall n \in \{1, 2, \dots, N\}$. It is observed from Fig. 4 that the derived waveforms align well with the exact solutions for the cases $N = 1, 2, 4, 8$, validating the efficacy of our signal model. However, when $N = 16$ or $N = 32$, the theoretical waveforms slightly deviate from the exact solutions. This derivation stems from the narrow instantaneous bandwidth of a RARE [34]. Specifically, when N is small, the maximum IF (e.g., $\delta_8/2\pi = 800$ kHz for $N = 8$) is within the maximum instantaneous bandwidth of a RARE (typically $1 \sim 10$ MHz [34]). In this context, the quantum state ρ_{12} will have adequate time to converge to the steady-state solution derived in (11). On the contrary, as N increases, the maximum IF (e.g., $\delta_{32}/2\pi = 3.2$ MHz) gradually approaches the maximum instantaneous bandwidth of a RARE, resulting in insufficient time for the electron transition to reach a steady state. This discrepancy causes the exact solution to deviate from the theoretical model. Overall,

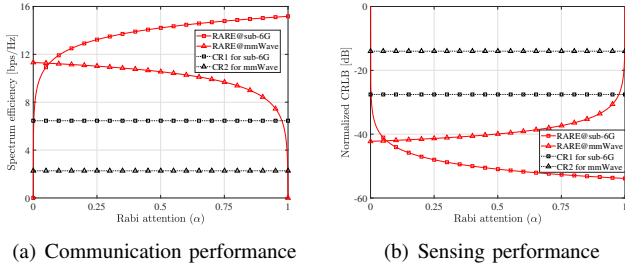


Figure 5. C&S performance at different frequency bands for different settings of Rabi attention, α .

the derived signal transmission model precisely captures the dynamics of multi-level electron transitions when the signal bandwidth falls within the detectable instantaneous bandwidth of a RARE.

C. Performance of Multi-Band RAREs

In this subsection, we evaluate multi-band C&S performance by comparing the multi-band RARE with a classic sub-6G receiver, CR1, and a classic mmWave receiver, CR2. The communication performance is quantified by the SE while the sensing performance is assessed using the NCRLB.

Fig. 5 evaluates the C&S performance under varying Rabi attentions. Specifically, the Rabi attentions for the two bands are expressed as $\alpha_1 = \alpha$ and $\alpha_2 = 1 - \alpha$, with α ranging from 0 to 1. As observed in Fig. 5, the C&S performance at the sub-6G band achieved by the multi-band RARE continuously improves with increasing α , whereas the performance at the mmWave band consistently declines. This is attributed to the attention mechanism of the multi-band RARE, where α characterizes the proportion of sensitivity allocated to the sub-6G band. Notably, when $\alpha = 1$, the multi-band RARE simplifies to the existing single-band RARE. In this case, the C&S performance at the sub-6G band is maximized, yielding an SE of 15 bps/Hz and an NCRLB of -52 dB. However, the C&S services at the mmWave band are broken. Conversely, setting $\alpha = 0.5$ results in a negligible degradation in the sub-6G performance (a 1 bps/Hz reduction in SE and 2 dB increase in NCRLB), while the mmWave band experiences a significant improvement, with the SE increasing from 0 bps/Hz to 10.5 bps/Hz and the NCRLB reducing from infinity to -40 dB. This example demonstrates the superiority of multi-band RARE over single-band RARE in addressing heterogeneous C&S tasks. Furthermore, the multi-band RARE achieves a remarkable C&S performance gain compared to the two classic receivers, provided that the Rabi attention is appropriately configured. For instance, when $\alpha = 0.25$, there is an average increase of 7 bps/Hz in SE and a 30 dB decrease in NCRLB. It is noteworthy that all these multi-band C&S performance gains are achieved within a single RARE device.

Then, we evaluate the effects of Rabi sum-square on the achieved SE in Fig. 6(a) and on the NCRLB in Fig. 6(b), both averaged on the two frequency bands. In addition to the performance achieved by two classic receivers, denoted as “CR1&CR2”, we also include the multi-band RARE with

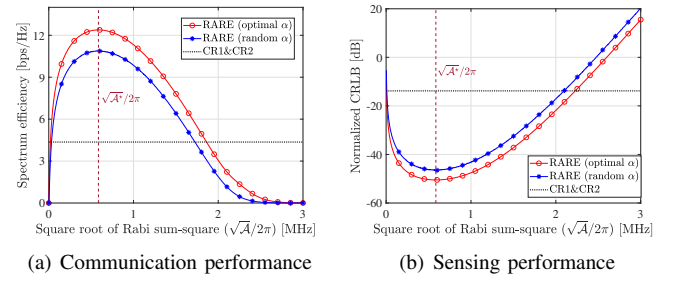


Figure 6. Comparison between the multi-band RAREs and classic receivers for different settings of Rabi sum-square, \mathcal{A} .

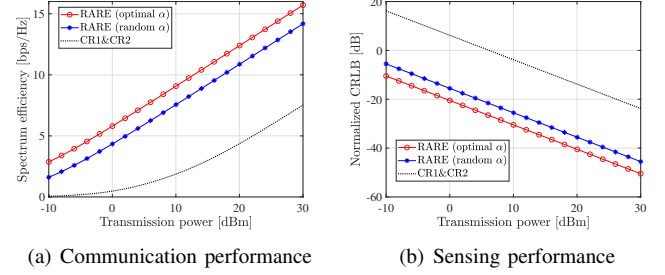


Figure 7. Comparison between the multi-band RAREs and classic receivers for different settings of the transmission power, P_{tx} .

randomly sampled Rabi attentions, $\alpha \sim \mathcal{U}(0, 0.5)$, as a benchmark. As the Rabi sum-square \mathcal{A} increases, the performance of RAREs initially improves, but then declines. This trade-off can be interpreted by the electron transition process. Specifically, when Rabi frequency of the reference signal is either small or large, all electrons are predominantly located in either the initial Rydberg state or final Rydberg state. In both of these scenarios, the Rydberg atom is unable to effectively respond to the weak wireless data signal. Sensitivity to the weak signal is achieved only when the Rabi frequency of the reference signal is moderate enough for approximately half of the electrons to be situated in the final Rydberg state. Nevertheless, the derived optimal Rabi sum-square, $\sqrt{\mathcal{A}^*} = 2\pi \times 0.586$ MHz, can consistently capture the most sensitive state of a RARE, regardless of the values of Rabi attentions or the conducted C&S services. This is due to the fact that the Rabi sum-square only influences the global gain, ϱ_0 , amplified on all frequency bands, thereby uniformly enhancing the sensitivity of a RARE to all frequency bands. Using the optimal Rabi sum-square and Rabi attentions, a RARE can outperform classic receivers by 7.5 bps/Hz in SE and by 35 dB in NCRLB. This verifies the necessity for the optimization of Rabi sum-square to maximize the sensitivity.

Finally, Fig. 7 illustrates the C&S performance as a function of the transmission power, $P_{tx,n}$, spanning from -10 dBm to 30 dBm. The optimal Rabi sum-square is adopted for both “RARE (optimal α)” and “RARE (random α)”. As depicted in Fig. 7, the multi-band RAREs significantly outperform classic receivers in all considered transmission power. Furthermore, compared to the benchmark of “RARE (random α)”, the optimal design of Rabi attentions further improves the SE by 1.5 bps/Hz and reduces the NCRLB by 5 dB. This result underscores the critical importance of optimizing Rabi attentions for each communication or sensing task.

VI. CONCLUSIONS

In this paper, we have unveiled the underlying physical mechanisms of multi-band RAREs, representing a significant advancement in multi-band wireless C&S. The transfer function of multi-band RAREs is derived by solving the closed-form expression for the quantum response of Rydberg atoms excited by multi-band RF signals. Our findings reveal that a multi-band RARE functions as both a multi-band atomic mixer and a multi-band atomic amplifier. Additionally, the attention mechanism of the multi-band atomic amplifier was elucidated. We have also presented globally optimal designs for the gain factors of the atomic amplifier to maximize the receiver sensitivity and the overall C&S performance. Numerical results confirmed the effectiveness of the derived transfer function and the superiority of multi-band RAREs.

We conclude this paper by outlining potential avenues for future research. To begin with, the derivation presented assumes that the frequency of each band resonates with the corresponding electron transition. However, understanding the quantum response of multi-band RAREs under *off-resonant* conditions remains an open problem. Moreover, leveraging the multi-band capability to protect data privacy is a promising direction. Finally, the multi-band RARE can be incorporated with the atomic multiple-input-multiple-output (MIMO) technique [9], [35] to further improve wireless C&S performance.

APPENDIX

A. Steady-state solutions of ρ

We use $\rho_{mn}, \forall m, n \in \{1, 2, 3, 4, 5\}$ to denote the (m, n) -th entry of ρ . The steady-state solutions of each entry to the equation (6) are given as

$$\begin{aligned}\rho_{11} &= \frac{(\Omega_p^2 + \gamma_2^2)(\Omega_1^2 + \Omega_2^2) + \Omega_c^2 \Omega_p^2}{(\gamma_2^2 + 2\Omega_p^2)(\Omega_1^2 + \Omega_2^2) + 2\Omega_p^2(\Omega_c^2 + \Omega_p^2)}, \\ \rho_{12} &= j \frac{\gamma_2 \Omega_p (\Omega_1^2 + \Omega_2^2)}{(\gamma_2^2 + 2\Omega_p^2)(\Omega_1^2 + \Omega_2^2) + 2\Omega_p^2(\Omega_c^2 + \Omega_p^2)}, \\ \rho_{13} &= - \frac{\Omega_c \Omega_p^3}{(\gamma_2^2 + 2\Omega_p^2)(\Omega_1^2 + \Omega_2^2) + 2\Omega_p^2(\Omega_c^2 + \Omega_p^2)}, \\ \rho_{14} &= -j \frac{\gamma_2 \Omega_1 \Omega_c \Omega_p}{(\gamma_2^2 + 2\Omega_p^2)(\Omega_1^2 + \Omega_2^2) + 2\Omega_p^2(\Omega_c^2 + \Omega_p^2)}, \\ \rho_{15} &= -j \frac{\gamma_2 \Omega_2 \Omega_c \Omega_p}{(\gamma_2^2 + 2\Omega_p^2)(\Omega_1^2 + \Omega_2^2) + 2\Omega_p^2(\Omega_c^2 + \Omega_p^2)}, \\ \rho_{22} &= \frac{\Omega_p^2 (\Omega_1^2 + \Omega_2^2)}{(\gamma_2^2 + 2\Omega_p^2)(\Omega_1^2 + \Omega_2^2) + 2\Omega_p^2(\Omega_c^2 + \Omega_p^2)}, \\ \rho_{24} &= - \frac{\Omega_1 \Omega_c \Omega_p^2}{(\gamma_2^2 + 2\Omega_p^2)(\Omega_1^2 + \Omega_2^2) + 2\Omega_p^2(\Omega_c^2 + \Omega_p^2)}, \\ \rho_{25} &= - \frac{\Omega_2 \Omega_c \Omega_p^2}{(\gamma_2^2 + 2\Omega_p^2)(\Omega_1^2 + \Omega_2^2) + 2\Omega_p^2(\Omega_c^2 + \Omega_p^2)}, \\ \rho_{33} &= \frac{\Omega_p^4}{(\gamma_2^2 + 2\Omega_p^2)(\Omega_1^2 + \Omega_2^2) + 2\Omega_p^2(\Omega_c^2 + \Omega_p^2)},\end{aligned}$$

$$\begin{aligned}\rho_{44} &= \frac{\Omega_1^2 \Omega_p^2 (\Omega_p^2 + \Omega_c^2)}{(\gamma_2^2 + 2\Omega_p^2)(\Omega_1^2 + \Omega_2^2)^2 + 2\Omega_p^2(\Omega_c^2 + \Omega_p^2)(\Omega_1^2 + \Omega_2^2)}, \\ \rho_{55} &= \frac{\Omega_2^2 \Omega_p^2 (\Omega_p^2 + \Omega_c^2)}{(\gamma_2^2 + 2\Omega_p^2)(\Omega_1^2 + \Omega_2^2)^2 + 2\Omega_p^2(\Omega_c^2 + \Omega_p^2)(\Omega_1^2 + \Omega_2^2)}, \\ \rho_{45} &= \frac{\Omega_1 \Omega_2 \Omega_p^2 (\Omega_p^2 + \Omega_c^2)}{(\gamma_2^2 + 2\Omega_p^2)(\Omega_1^2 + \Omega_2^2)^2 + 2\Omega_p^2(\Omega_c^2 + \Omega_p^2)(\Omega_1^2 + \Omega_2^2)}, \\ \rho_{23} &= \rho_{34} = \rho_{35} = 0.\end{aligned}$$

For the elements, ρ_{mn} with $m > n$, they can be obtained as $\rho_{mn} = \rho_{nm}^*$ since the matrix ρ is Hermitian.

B. Proof of Theorem 2

Problem (33) is equivalent to maximizing the function $f(\mathcal{A}) = \exp\left(-\frac{\chi_0 \mathcal{A}}{\mathcal{A} + \Gamma^2}\right) \frac{\mathcal{A}}{(\mathcal{A} + \Gamma^2)^4}$ with $\mathcal{A} > 0$. To solve it, we introduce the variable transformation $x = \frac{\mathcal{A}}{\mathcal{A} + \Gamma^2}$. Then, we get $0 \leq x < 1$ and $\mathcal{A} = \frac{x}{1-x} \Gamma^2$. The function $f(\mathcal{A})$ can thus be rewritten as

$$f(\mathcal{A}) = \frac{1}{\Gamma^6} e^{-\chi_0 x} x (1-x)^3 \triangleq g(x). \quad (49)$$

The gradient of $g(x)$ is given as

$$\frac{dg(x)}{dx} = \frac{1}{\Gamma^6} e^{-\chi_0 x} (1-x^2)(\chi_0 x^2 - (\chi_0 + 4)x + 1). \quad (50)$$

By setting $\frac{dg(x)}{dx} = 0$ and doing some tedious calculations, we can obtain the optimal x that maximizes $g(x)$ in the range $x \in [0, 1]$ as

$$x^* = \frac{\chi_0 + 4 - \sqrt{\chi_0^2 + 4\chi_0 + 16}}{2\chi_0}. \quad (51)$$

When $0 \leq x < x^*$, the gradient $\frac{dg(x)}{dx}$ is greater than 0 and thus $g(x)$ monotonically increases, while when $x^* < x < 1$, the gradient $\frac{dg(x)}{dx}$ is smaller than 0 and thus $g(x)$ monotonically decreases,

By further invoking the relationship $\mathcal{A} = \frac{x}{1-x} \Gamma^2$. The optimal Rabi sum-square is thus given as

$$\mathcal{A}^* = \frac{\chi_0 + 4 - \sqrt{\chi_0^2 + 4\chi_0 + 16}}{\chi_0 - 4 + \sqrt{\chi_0^2 + 4\chi_0 + 16}} \Gamma^2. \quad (52)$$

This completes the proof.

C. Proof of Theorem 3

The Lagrange function of problem (40) is given as

$$\mathcal{L} = \sum_{n=1}^N \gamma_n \log_2 \left(1 + \frac{\beta_n \alpha_n}{\alpha_n + \epsilon_n} \right) + \frac{1}{\nu} \left(1 - \sum_{n=1}^N \alpha_n \right). \quad (53)$$

Here, ν is the Lagrange multiplier and we adopt its reciprocal form $1/\nu$ for ease of later expression. The KKT conditions are given as

$$\frac{\partial \mathcal{L}}{\partial \alpha_n} = \frac{\gamma_n \beta_n \epsilon_n}{((1 + \beta_n) \alpha_n + \epsilon_n)(\alpha_n + \epsilon_n)} - \frac{1}{\nu} = 0, \forall n \quad (54)$$

$$\sum_{n=1}^N \alpha_n = 1. \quad (55)$$

The condition in (54) follows a quadratic form. As $\alpha_n \geq 0$, we have $\frac{\gamma_n \beta_n \epsilon_n}{((1+\beta_n)\alpha_n + \epsilon_n)(\alpha_n + \epsilon_n)} > 0$. Therefore, the Lagrange multiplier ν must greater than 0 as well. Otherwise there will be no feasible solutions to (54) for all n . Given $\nu \geq 0$, the solutions of these quadratic equations should obey

$$\alpha_n = \frac{-(2 + \beta_n)\epsilon_n \pm \sqrt{\beta_n^2 \epsilon_n^2 + 4\nu\gamma_n\beta_n(1 + \beta_n)\epsilon_n}}{2(1 + \beta_n)}. \quad (56)$$

By further considering the requirement $\alpha_n \geq 0$, the solution of $\frac{-(2 + \beta_n)\epsilon_n - \sqrt{\beta_n^2 \epsilon_n^2 + 4\nu\gamma_n\beta_n(1 + \beta_n)\epsilon_n}}{2(1 + \beta_n)}$ should be discarded as it is smaller than 0. Besides, the other one needs to be modified as

$$\alpha_n^* = \left(\frac{-(2 + \beta_n)\epsilon_n + \sqrt{\beta_n^2 \epsilon_n^2 + 4\nu^*\gamma_n\beta_n(1 + \beta_n)\epsilon_n}}{2(1 + \beta_n)} \right)^+, \quad (57)$$

where $(x)^+ \triangleq \max(0, x)$. The optimal Lagrange multiplier ν^* is properly selected to satisfy the constraint $\sum_{n=1}^N \alpha_n = 1$. This completes the proof.

REFERENCES

- [1] B. Liu, L. Zhang, Z. Liu, Z. Deng, D. Ding, B. Shi, and G. Guo, "Electric field measurement and application based on Rydberg atoms," *Electromagn. Sci.*, vol. 1, no. 2, pp. 1–16, Jun. 2023.
- [2] M. Cui, Q. Zeng, and K. Huang, "Rydberg atomic receiver: Next frontier of wireless communications," *arXiv preprint arXiv:2412.12485*, Dec. 2024.
- [3] S. S. A. Yuan, X. Y. I. Xu, J. Yuan, G. Xie, C. Huang, X. Chen, Z. Huang, and W. E. I. Sha, "Electromagnetic modeling and capacity analysis of Rydberg atom-based MIMO system," *IEEE Antennas Wireless Propag. Lett.*, pp. 1–5, 2025.
- [4] C. T. Fancher, D. R. Scherer, M. C. S. John, and B. L. S. Marlow, "Rydberg atom electric field sensors for communications and sensing," *IEEE Trans. Quantum Eng.*, vol. 2, no. 3501313, pp. 1–13, Mar. 2021.
- [5] Y. Chen, X. Guo, C. Yuen, Y. Zhao, Y. Guan, C. M. S. See, M. Debbah, and L. Hanzo, "Harnessing Rydberg atomic receivers: From quantum physics to wireless communications," *arXiv preprint arXiv:2501.11842*, Jan. 2025.
- [6] G. Gao, M. Chen, H. Feng, Z. Zhu, A. Chen, Z. Wu, T. Mao, W. Dai, P. Peng, and D. Zheng, "Rydberg communication antennas with self-decoupling for dynamic radar interference based on heterodyne technology," *Appl. Phys. Lett.*, vol. 126, no. 13, p. 134002, Apr. 2025.
- [7] H. Zhang, Y. Ma, K. Liao, W. Yang, Z. Liu, D. Ding, H. Yan, W. Li, and L. Zhang, "Rydberg atom electric field sensing for metrology, communication and hybrid quantum systems," *Sci. Bull.*, vol. 69, no. 10, pp. 1515–1535, May 2024.
- [8] F. Zhang, B. Jin, Z. Lan, Z. Chang, D. Zhang, Y. Jiao, M. Shi, and J. Xiong, "Quantum wireless sensing: Principle, design and implementation," in *Proc. Annu. Int. Conf. Mobile Comput. Netw. (ACM MobiCom'23)*, Oct. 2023, pp. 1–15.
- [9] M. Cui, Q. Zeng, and K. Huang, "Towards atomic MIMO receivers," *IEEE J. Sel. Areas Commun.*, vol. 43, no. 3, pp. 659–673, 2025.
- [10] M. Cui, Q. Zeng, Z. Wang, and K. Huang, "Realizing quantum wireless sensing without extra reference sources: Architecture, algorithm, and sensitivity maximization," *arXiv preprint arXiv:2504.21234*, Apr. 2025.
- [11] B. Xu, J. Zhang, Z. Chen, B. Cheng, Z. Liu, Y.-C. Wu, and B. Ai, "Channel estimation for Rydberg atomic receivers," *arXiv preprint arXiv:2503.08985*, Mar. 2025.
- [12] H. Kim, H. Park, and S. Kim, "Quantum-MUSIC: Multiple signal classification for quantum wireless sensing," *IEEE Wireless Commun. Lett.*, 2025.
- [13] H. Wu, X. Yao, C. Xie, K.-D. Wu, S. Wu, R. Ni, G.-Y. Xiang, and C. Gong, "On-off keying signal detection based on hidden markov model for Rydberg atomic sensor," *IEEE Trans. Commun.*, 2025.
- [14] Z. Liu, L. Zhang, B. Liu, Z. Zhang, G. Guo, D. Ding, and B. Shi, "Deep learning enhanced Rydberg multifrequency microwave recognition," *Nat. Commun.*, vol. 13, no. 1, p. 1997, Apr. 2022.
- [15] H. Nyquist, "Thermal agitation of electric charge in conductors," *Phys. Rev.*, vol. 32, no. 1, pp. 110–113, Jul. 1928.
- [16] T. Gong, J. Sun, C. Yuen, G. Hu, Y. Zhao, Y. Guan, C. M. S. See, M. Debbah, and L. Hanzo, "Rydberg atomic quantum receivers for classical wireless communications and sensing: Their models and performance," *arXiv preprint arXiv:2412.05554*, Dec. 2024.
- [17] T. Gong, A. Chandra, C. Yuen, Y. L. Guan, R. Dumke, C. M. S. See, M. Debbah, and L. Hanzo, "Rydberg atomic quantum receivers for classical wireless communication and sensing," *IEEE Wireless Commun.*, pp. 1–11, 2025.
- [18] L. J. Chu, "Physical limitations of omni-directional antennas," *J. Appl. Phys.*, vol. 19, no. 12, pp. 1163–1175, Dec. 1948.
- [19] C. Holloway, M. Simons, A. H. Haddab, J. A. Gordon, D. A. Anderson, G. Raithel, and S. Voran, "A multiple-band Rydberg atom-based receiver: AM/FM stereo reception," *IEEE Antennas Propag. Mag.*, vol. 63, no. 3, pp. 63–76, Jun. 2021.
- [20] Y. Du, N. Cong, X. Wei, X. Zhang, W. Luo, J. He, and R. Yang, "Realization of multiband communications using different Rydberg final states," *AIP Adv.*, vol. 12, no. 6, p. 065118, Jun. 2022.
- [21] D. H. Meyer, J. C. Hill, P. D. Kunz, and K. C. Cox, "Simultaneous multiband demodulation using a Rydberg atomic sensor," *Phys. Rev. Appl.*, vol. 19, p. 014025, Jan. 2023.
- [22] L.-H. Zhang, B. Liu, Z.-K. Liu, Z.-Y. Zhang, S.-Y. Shao, Q.-F. Wang, Y. Ma, T.-Y. Han, G.-C. Guo, D.-S. Ding, and B.-S. Shi, "Ultra-wide dual-band rydberg atomic receiver based on space division multiplexing radio-frequency chip modules," *Chip*, vol. 3, no. 2, p. 100089, Jun. 2024.
- [23] G. Allinson, M. J. Jamieson, A. R. Mackellar, L. Downes, C. S. Adams, and K. J. Weatherill, "Simultaneous multiband radio-frequency detection using high-orbital-angular-momentum states in a Rydberg-atom receiver," *Phys. Rev. Res.*, vol. 6, p. 023317, Jun. 2024.
- [24] S. You, M. Cai, H. Zhang, Z. Xu, and H. Liu, "Exclusive effect in Rydberg atom-based multi-band microwave communication," *Photonics*, vol. 10, no. 3, Mar. 2023.
- [25] W. Wen, S. Yan, R. Wang, X. Li, J. Tan, X. Pang, W. Zhai, W. Cui, and Y. Gao, "Rydberg-atom-based multiband frequency-hopping communication receiver using five-level atomic system," *Opt. Express*, vol. 32, no. 24, pp. 42 872–42 884, Nov. 2024.
- [26] H. Kim, H. Park, J. Won, and S. Kim, "Multi-band quantum wireless sensing for Rydberg atomic receivers," *IEEE Commun. Lett.*, 2025.
- [27] S. Parkvall, E. Dahlman, A. Furuskar, and M. Frenne, "NR: The new 5G radio access technology," *IEEE Commun. Standards Mag.*, vol. 1, no. 4, pp. 24–30, Dec. 2017.
- [28] M. S. Sim, Y.-G. Lim, S. H. Park, L. Dai, and C.-B. Chae, "Deep learning-based mmWave beam selection for 5G NR/6G with sub-6 GHz channel information: Algorithms and prototype validation," *IEEE Access*, vol. 8, pp. 51 634–51 646, 2020.
- [29] C. J. Foot, *Atomic Physics*. Oxford University Press, 2005.
- [30] M. Jing, Y. H. Hu, J. Ma, H. Zhang, L. Zhang, L. Xiao, and S. Jia, "Atomic superheterodyne receiver based on microwave-dressed Rydberg spectroscopy," *Nat. Phys.*, vol. 1, pp. 911–915, Jun. 2020.
- [31] X.-H. Liu, K.-Y. Liao, Z.-X. Zhang, H.-T. Tu, W. Bian, Z.-Q. Li, S.-Y. Zheng, H.-H. Li, W. Huang, H. Yan, and S.-L. Zhu, "Continuous-Frequency Microwave Heterodyne Detection in an Atomic Vapor Cell," *Phys. Rev. Appl.*, vol. 18, no. 5, p. 054003, Nov. 2022, publisher: American Physical Society.
- [32] S. Boyd and L. Vandenberghe, *Convex Optimization*. Cambridge University Press, 2004.
- [33] N. Šibalić, J. Pritchard, C. Adams, and K. Weatherill, "ARC: An open-source library for calculating properties of alkali Rydberg atoms," *Comput. Phys. Commun.*, vol. 220, pp. 319–331, Nov. 2017.
- [34] Z. Jia, Q. Li, Y. Wang, Y. You, B. Chen, and Y. Peng, "Properties and utilization in time-dependent Rydberg EIT," *Opt. Continuum*, vol. 3, no. 2, pp. 135–147, Feb. 2024.
- [35] M. Cui, Q. Zeng, and K. Huang, "MIMO precoding for Rydberg atomic receivers," *arXiv preprint arXiv:2408.14366*, Aug. 2024.